First-principles models for phase stability and radiation defects in structural materials for future fusion power-plant applications

D. Nguyen-Manh*, M.Yu. Lavrentiev, M. Muzyk, S.L. Dudarev

EURATOM/CCFE Fusion Association, Culham Science Centre, Abingdon, Oxfordshire, OX14 3DB, UK

* Tel: +44 1235 466284, Fax: +44 1235 466435, Email: duc.nguyen@ccfe.ac.uk

Abstract Generic materials-related problems foreseen in connection with the operation of a fusion power plant present a major challenge for the development of magnetically confined fusion as a commercial power generation option. In this review, we focus on the predictive capabilities of first-principles-based atomistic models for radiation defects and phase stability of body-centred cubic Fe-Cr-based ferritic-martensitic and ferritic steels and tungsten alloys, which are presently under consideration as candidate structural materials for the first wall and divertor applications. Density functional calculations predict that low-Cr iron alloys are stabilized by intra-atomic exchange, giving rise to magnetism and changes in interatomic chemical bonding. Magnetic effects are also responsible for the fact that the atomic structure of radiation defects in iron and steels is different from the structure of defects formed under irradiation in non-magnetic body-centered cubic metals, for example vanadium or tungsten. *Ab initio*-based magnetic cluster expansion-based Monte-Carlo simulations showed unusual non-collinear magnetic configurations forming at interfaces and around Cr precipitates in FeCr alloys. In W-Ta and W-V alloys, *ab initio* calculations helped identify several low temperature ordered inter-metallic phases that are not included in the existing phase diagrams based on high-temperature experimental data. *Ab initio* calculations have also made it possible to predict atomic structures of point defects formed in these alloys under irradiation.

Keywords: nuclear fusion materials, ab initio calculations, phase stability, irradiated defects, magnetic properties

Introduction

The economic viability of operation of a fusion power plant fundamentally depends on the availability of materials able to retain their properties under irradiation by the 14 MeV neutrons generated by burning deuterium-tritium plasma. The development of fusion reactor materials is a subject of extensive international effort, which includes production and testing of materials under simulated irradiation conditions, in fission reactors or under fusion-like spectrum of neutrons generated by an accelerator-based International Fusion Materials Irradiation Facility (IFMIF), the concept of which is presently undergoing engineering evaluation and design [1]. Another, equally significant, part of fusion materials programme is the development of predictive mathematical modelling capabilities aimed at rationalising the extensive already available experimental information on properties of irradiated fusion materials, as well as information coming from ion beam irradiation experiments, to predict the behaviour of materials under fusion-relevant conditions not yet accessible to experimental tests. In design studies of fusion power plants and next generation fusion devices, such as DEMO (see Fig. 1), ferritic-martensitic and ferritic steels are considered as candidate materials for the structural components of the first wall and the breeding blanket because in the limit of high irradiation dose these steels exhibit significantly lower swelling than austenitic steels, with oxide dispersion strengthened ferritic steels retaining acceptable tensile strength at temperatures close to 700ºC [2]. Both types of steels are ferromagnetic, and their Curie temperatures are close to the expected range of operating temperatures of the power plant. At the same time, tungsten and tungsten alloys are among the

candidate materials for plasma-facing components (PFCs) in the DEMO design, in particular for high-heat-flux regions such as the divertor [3].

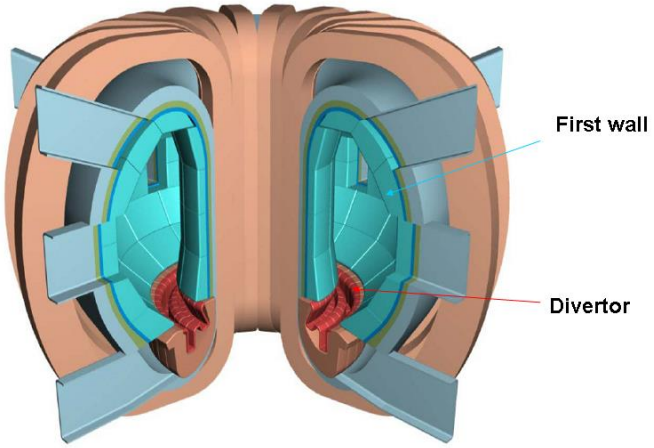

Fig.1. Schematic diagram of a fusion power plant showing the first wall and divertor.

The expected performance of plasma-facing components, components of the first wall, and blanket systems of future fusion power presents various multi-scale computational challenges that can only be addressed using high-performance computing. In this paper, we review how computational methods based on first-principles calculations can elucidate several key properties of Fe-Cr based ferric steels and W-alloys, encompassing phase stability and chemical bonding as well as the structure of defects formed under irradiation. Our study is a part of a broader program of work aimed at finding out how the choice of chemical composition and microstructure is related to properties of materials, and how the properties vary as a result of exposure to fusion neutron irradiation. Using *ab initio* calculations, we attempt to rationalize systematic trends characterizing phase stability, point defects, and elastic properties of concentrated iron and tungsten alloys, as a step toward modelling larger-scale micro-structural features, including grain boundaries, dislocations, and dislocation ensembles. First-principles calculations provide information about microscopic phenomena, the understanding of which is required for the development of larger-scale models, for example molecular dynamics and Monte Carlo simulations.

The paper is organized as follows. In the second section, we describe computational methods based on density functional theory calculations. In particular, our discussions focus on many-body Hamiltonian models as well as on Magnetic Cluster Expansion approach. In the third section, we highlight the systematic trend exhibited by point defects in bcc transition metals, assessing it from the electronic structure point of view. In the fourth section, we review the phase stability of magnetic Fe-Cr based alloys and W-Ta and W-V binary alloys. In the fifth section, we discuss how information about properties of point defects, derived from first-principles calculations of alloys, is used as input for large scale kinetic Monte Carlo simulations. The last section summarizes the results and concludes the paper.

Computational methodologies

Density Functional Theory methods

First-principles calculations described in this work were performed within density functional theory (DFT) implemented in the Package of Linear combination of Atomic Type Orbitals (PLATO) code using atomic-like basis sets [4-6] and in the Vienna Ab-initio Simulation Package (VASP) code that uses plane-wave basis sets [7-9]. More information about technical details of these calculations can be found in [10-11]. In both codes, the Perdew–Burke–Ernzerhof (PBE) generalized gradient approximation (GGA) [12] is used for describing the effects of exchange and correlation functional, with semi-core electrons included through the use of pseudo-potentials. It is important to emphasize that the inclusion of *semi-core electrons* in the valence states has a significant effect on the predicted formation energies of self-interstitial atom (SIA) defects for all the bcc transition metals [4,13]. In particular, we find that the most stable <111> configuration of SIAs cannot be reproduced correctly if the semi-core electrons are ignored, this is especially significant for transition metals of group 6B (Cr, Mo, W). There is overall good agreement between PLATO and VASP predictions of defect formation energies and the structure-energy trends exhibited by various SIAs configurations.

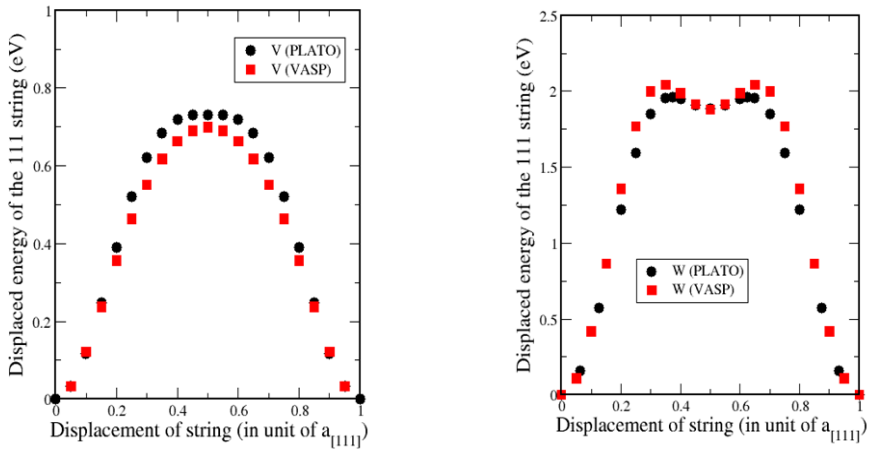

Fig.2. Curves, computed using DFT, and showing variation of energy per Burgers vector of translation in the (111) direction, associated with a rigid translation of a (111) string of atoms through the lattice in bcc vanadium and bcc tungsten. DFT calculations were performed using PLATO and VASP codes.

To ensure that DFT results are code-independent, we show in Fig. 2 the results of benchmarking *ab initio* calculations of "lattice potentials" corresponding to the translation of a (111) string of atoms in the direction parallel to the string itself, for two bcc transition metals of groups 5B (vanadium) and 6B (tungsten) of the periodic table. Computations were performed using PLATO and VASP packages. Plato is a general-purpose total energy electronic structure code that represents single particle electronic wave functions in terms of an expansion in terms of atomic type orbitals. The orbitals are not expanded in analytic functions, but rather are finite in range and represented by a numerical radial mesh multiplied by spherical harmonics. The choice of atomic orbitals makes available a range of approximate techniques. Plato can be used to model the properties of solids, liquids and molecules. The relaxation of atoms can be performed using the usual algorithms (steep descent, conjugate gradient, variable metric). When both the cell

coordinates and atomic coordinates are relaxed simultaneously, the atomic coordinates are relaxed first, then the cell is allowed to relax, followed by the atoms again etc. This nested approach was found to greatly improve the stability of the relaxation. The vast majority of the effort involved in the evaluation of the matrix elements and the calculation of the energy, the forces and the stress is parallelised.

In PLATO code, we employed relativistic semicore separable pseudo-potentials developed by Hartwigsen et al. [14] whereas in the VASP code we used projected augmented wave (PAW) potentials with the plane-wave energy cut-off of 400 eV, sufficient for total energy convergence. Fig.2 shows a group-specific trend in the potentials, both in terms of the shape and the predicted energy of the central point. For all the bcc metals of group 5B, DFT calculations show the same structure of a flat peak, whereas a structure with a local minimum is characteristic of the metals in group 6B. We have combined density-functional calculations of the <111> string potential profile with an extended version of the analytical Frenkel-Kontorova model to reveal important underlying differences between the metals in these groups, which are not accessible to either the numerical or analytical approaches alone. The difference between the string displacement energy curves accounts for the previously unexplained significantly higher crowdion migration temperatures observed in metals of group 6B relative to those of group 5B [15] and explains the observed large differences in the crowdion migration temperatures between groups 5B and 6B, as observed in the resistivity recovery experiments [16].

Cluster Expansion formalism and Monte-Carlo method

The structural phase stability of binary alloys was investigated using the cluster expansion (CE) formalism [17], in which the formation enthalpy of an alloy configuration is mapped onto an Ising-like Hamiltonian involving a set of multi-site effective interaction parameters {J}

$$H_{DFT}(\{\sigma\}) = J_0 + \sum_i J_i \sigma_i + \sum_{ij} J_{ij} \sigma_i \sigma_j + \sum_{ijk} J_{ijk} \sigma_i \sigma_j \sigma \quad (1)$$

For a binary system, the occupation variable $\{\sigma\}$, whose components are $\sigma_i=\pm 1$, indicates whether a lattice site is occupied by an atom of type A or B. The CE coefficients {J} are normally obtained using iterated fitting to a DFT database derived from total energy calculations and containing more than 150 bcc-like structures for each binary alloy. A cross-validation error is of the order of 3.5 meV/atom averaged over all the configurations included in the fit for W-Ta and W-V alloys. The final sets of the calculated effective cluster interaction (ECI) parameters for Fe-Cr alloys are published in [18], and for W-Ta and W-V alloys they are published in [19]. These ECI were then used in semi-grand canonical Monte-Carlo calculations in order to investigate the enthalpy of mixing and chemical short range order as a function of temperature. Monte-Carlo simulations were performed over a large range of temperatures starting from a fully disordered configuration, which was then cooled down to the low temperature region where various ground state configurations of ordered inter-metallic compounds in binaries W-Ta and W-V systems were found using DFT and CE predictions [19-20].

Many-body Stoner Hamiltonian

In order to understand magnetic properties of Fe-Cr based alloys, we have derived a model tight-binding many-body *d*-electron Stoner Hamiltonian and investigated the sensitivity of its mean-field solutions to the choice of hopping integrals and the Stoner exchange parameters [21]. This Hamiltonian has a general form [22-26]

$$\hat{H} = \sum_{i \neq j} \sum_{m,m',\sigma} t_{im,jm'} \hat{c}^{+}_{im\sigma} \hat{c}_{jm'\sigma} + \sum_{im\sigma} \varepsilon_{im\sigma} \hat{c}^{+}_{im\sigma} \hat{c}_{im\sigma}$$
$$+ \sum_i \left[\frac{\overline{U}_i}{2} \sum_{mm'\sigma} \hat{n}_{im\sigma} \hat{n}_{im'-\sigma} + \frac{\overline{U}_i - \bar{I}_i}{2} \sum_{mm'\sigma} \hat{n}_{im\sigma} \hat{n}_{im'\sigma} (1 - \delta_{mm'}) \right] \quad (2)$$

Interaction parameters $\overline{U}_i$ describe the Coulomb energy of repulsion between a pair of electrons occupying the same lattice site with anti-parallel spin whereas $\bar{I}_i$ described the reduction in the strength of Coulomb repulsion for the case where the spins of electrons are parallel. By applying the local charge-neutrality condition within a self -consistent treatment we showed that the intra-atom exchange parameters $\bar{I}_i$ of the multi-orbital periodic Anderson Hamiltonian (2) are exactly equal to the Stoner parameters [27-29]. Analysing the energy of solutions corresponding to model Hamiltonian (2) we found that the negative enthalpy-of-mixing anomaly characterizing the Fe-Cr alloy in the low chromium concentration limit [18, 30-31] is due entirely to the presence of the *on-site* exchange Stoner terms and that the occurrence of this anomaly is not specifically related to the choice of hopping integrals describing chemical bonding between atoms in the alloy. The Bain transformation pathway computed, using the model Hamiltonian above, for the $Fe_{15}Cr$ alloy configuration is in excellent agreement with *ab initio* total-energy calculations. Our investigation also shows how the parameters of a tight-binding many-body model Hamiltonian for a magnetic alloy can be derived from the comparison of its mean-field solutions with other, more accurate, mean-field approximations, for example DFT calculations, hence stimulating the development of larger-scale quantum-mechanical-based computational algorithms for modeling radiation damage effects in magnetic alloys and steels. The magnetic moment distributions showing 5 different sites of the σ-phase structure of Fe-40%Cr alloys is illustrated in Fig. 3, using the same scale for the tight-binding Stoner model based on Hamiltonian (2), and for DFT calculations. We find, using both methods, that magnetic moments on the two Cr sites (4f and 8j) are ordered anti-ferromagnetically in comparison with the moments situated on the three Fe sites [32]. Most recently, the tight-binding Stoner model was used for developing magnetic bond-order potentials for iron that not only reproduce correctly the relative stability of different magnetic bulk phases but also predict the behaviour of lattice defects such as dislocations that induce changes in bond lengths, bond angles, and local magnetic moments [33].

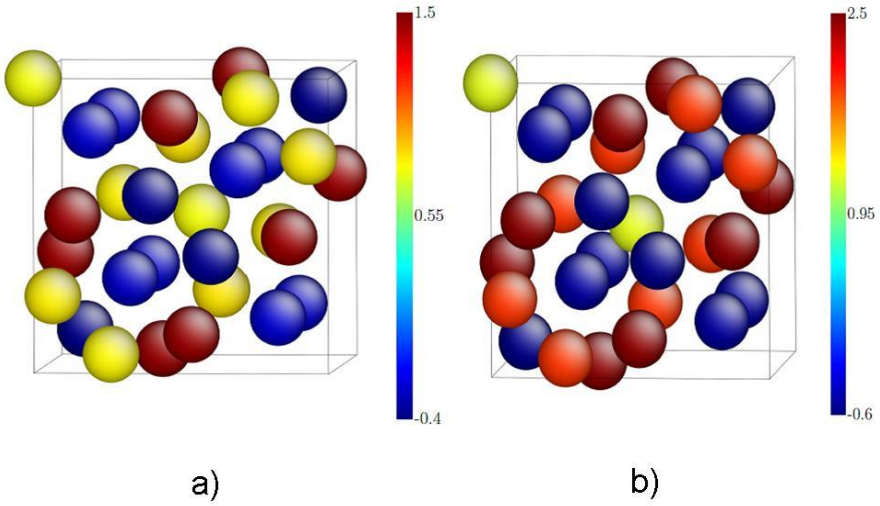

Fig.3 Comparison of DFT (a) and many-body Stoner Hamiltonian model (b) predictions for magnetic moments in Fe-Cr alloy in σ-phase at chromium concentration of 40% at. The colour code shows values of magnetic moment at 5 different crystallographic sites of the σ structure.

Magnetic Cluster Expansion

A new method for simulating structural phase stability of magnetic alloys, the magnetic cluster expansion (MCE) has been recently developed and applied to Fe-Cr based ferritic steels [34-35]

The energy of an alloy configuration in MCE depends both on the discrete CE occupational variables σ_i and on classical vector magnetic moments $\vec{M}_i$ of the constituent atoms. The moments of atoms have variable direction *and* magnitude. An MCE Hamiltonian contains the CE terms, the magnetic self-energy terms that determine the magnitude of magnetic moments, and inter-site Heisenberg-like magnetic interaction terms. The self-energy terms in the Hamiltonian are given by the sums of local atomic-configuration-dependent Landau terms quadratic and quartic in $\vec{M}_i$. In the implementation developed for FeCr alloys, we retained only two-atom clusters for both the non-magnetic and magnetic terms:

$$H^{MCE}(\{\sigma\},\{\vec{M}\}) = NJ^0 + I^1\sum_i \sigma_i + \sum_{ij} I_{ij}^2\sigma_i\sigma_j + \sum_i \left(A^0 + A^1\sigma_i + \sigma_i\sum_j A_{ij}^2\sigma_j \right)\vec{M}_i^{\,2}$$

$$+ \sum_i \left(B^0 + B^1\sigma_i + \sigma_i\sum_j B_{ij}^2\sigma_j \right)\vec{M}_i^{\,4} + \sum_{ij}\left[J_{ij}^0 + J_{ij}^1(\sigma_i + \sigma_J) + J_{ij}^2\sigma_i\sigma_j \right]\vec{M}_i\vec{M}_j \qquad (3)$$

Parameters of the model are determined at the MCE energy minimum, where an alloy configuration is matched to that found in DFT calculations:

$$\frac{\partial H^{MCE}(\{\sigma\},\{\vec{M}\})}{\partial \vec{M}_1}\Big|_{observed} = 0$$

$$\ldots \qquad (4)$$

$$\frac{\partial H^{MCE}(\{\sigma\},\{\vec{M}\})}{\partial \vec{M}_N}\Big|_{observed} = 0$$

Using MCE Hamiltonian, Monte Carlo simulations can then be performed to investigate finite-temperature magnetic properties of pure iron, as well as magnetic and structural properties of FeCr alloys. For example, the model predicts that the Curie temperature of a random Fe-Cr alloy increases in comparison with pure Fe in an interval of low Cr concentrations [36]. The method is also applied to the investigation of the non-collinear magnetic configurations formed on a large scale. Fig. 4 shows an optimized low energy magnetic configuration of the (100) interface between Fe (black atoms) and Cr (green atoms) found using the MCE model. The orientation of local magnetic moments agrees well with results of non-collinear spin-polarized DFT calculations [37].

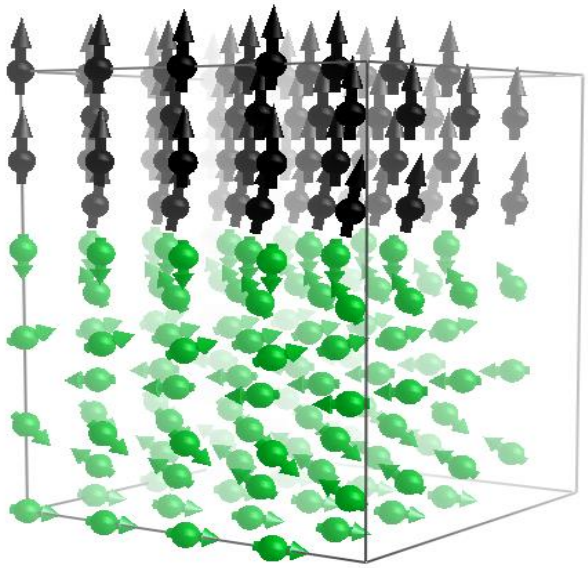

Fig. 4 MCE model prediction of non-collinear magnetism at the (100) Fe/Cr interface in the bulk of a concentrated FeCr alloy.

Radiation defect trends in transition metals

The need to identify the structure and formation energies of radiation defects in bcc transition metals and their alloys, including ferritic/martensitic steels, has recently received much attention since these metals are the main candidate structural materials not only for fusion [38] but also for advanced nuclear applications [39]. The energy of formation of self-interstitial atom (SIA) defects in bcc metals is several times the energy of formation of vacancies. Unlike vacancies, SIAs do not spontaneously form in materials at elevated temperatures. SIAs generated in high-energy collision cascades migrate to sinks in the material, and this gives rise to swelling, irradiation creep and radiation embrittlement. The small size and high mobility of individual SIA defects make them inaccessible to direct electron microscope observations. SIA defects are very remarkable because of the very large local strain field associated with their core. At the same time, until very recently there were no direct experimental data available on the formation energies of SIA defects. Quantitative insights into the ground state structures of SIAs and small clusters of SIA defects in all bcc transition metals were derived from density functional theory (DFT) calculations [4,10,13,40-41]. On one hand, in agreement with the orthorhombic long-range distortions observed using X-ray Huang diffuse scattering [42], a single SIA in iron has the structure of a <110> dumbbell. On another hand, our recent study of self-interstitial atom (SIA) defects in bcc transition metals show that in all the *non-magnetic* bcc transition metals, including bcc-W, the most stable defect configuration has the <111> (crowdion) orientation, in contradiction with earlier empirical potential results suggesting that the defects have the <110> orientation [43]. Importantly, further analysis based on the Peierls-Nabarro model for crowdion migration involving a combination of the double sine-Gordon model and DFT calculations showed that SIA migration temperatures for bcc-V and bcc-W were 8K and 30K [15, 44], in an excellent agreement with temperatures derived from experimental resistivity recovery measurements, which are 6K and 27K, respectively [16]. We would like to emphasise that SIA formation energy of 9.06±0.63 eV has been recently measured using low-temperature evaporation of tungsten in a field-ion microscope [45]. This value compares favourably with our earlier DFT prediction of 9.55 eV for SIA crowdion <111> configuration and 9.84 eV for the <110> dumbbell one. Most recently, the <111> crowdion SIA cluster configurations were observed using *in situ* electron transmission microscopy in bcc-Fe [46] and bcc-W [47].

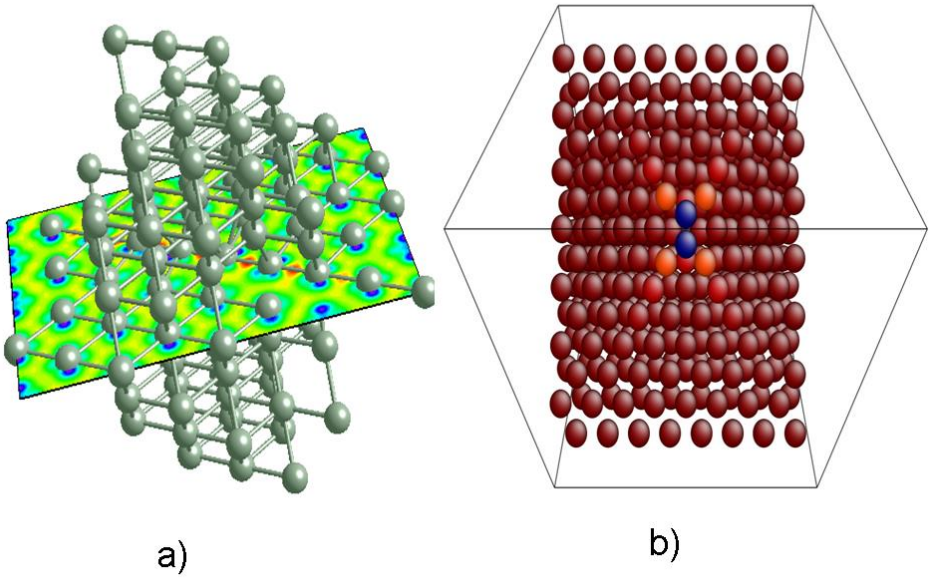

Fig.5. Crowdion <111> (a) and dumbbell <110> (b) defect configurations found using first-principles calculations. Figure shows both charge and spin density maps in bcc tungsten and iron, respectively. The core structure of crowdion is represented by the <111> string highlighted by the charge density change along this direction in bcc-W where as the core structure of the <110> dumbbell is shown by the two blue atoms with the opposite moments to the bcc-Fe host.

DFT calculations revealed that the pattern of ordering of SIA configurations is fundamentally different from that of ferromagnetic bcc Fe, where the <110> dumbbell has the lowest formation energy. Fig. 5 shows charge and spin density maps computed for two high-symmetry self-interstitial atom configurations, <111> in tungsten (5a) and <110>, in bcc ferromagnetic iron (5b), respectively. A <111> crowdion configuration shown in this figure, for which map of charge density difference between defect and perfect configurations is also shown in the figure, is formed by inserting an extra atom halfway between the nearest neighbours and by relaxing the resulting configuration. The now well established group-dependence of properties of defects in bcc transition metals has its origin in the electronic structure of materials. We have carried out a systematic study of the electronic local density of states (LDOS), deriving it from self-consistent DFT total energy calculations performed for the most stable SIA defects in bcc non-magnetic transition metals, i.e., for the <111> crowdion configuration and compared with those for the SIA <110> configuration in magnetic bcc-Fe [13] . Fig. 6a shows the LDOS calculated for atoms forming the central <111> string of crowdion configurations for all the bcc transition metals of groups 5B and 6B. For a fully relaxed supercell with 128+1 sites, there are five non-equivalent atoms in the central string containing the crowdion defect, starting with the atom at the centre of the crowdion (in Fig.6a, it is denoted as atom 0) to the atom situated at the end of the string (denoted as atom 4). In this figure, the position of the Fermi energy is shown by a vertical solid line. For an atom located sufficiently far away from the core of a crowdion (atom 4), the LDOS is shifted back to its bulk position where the Fermi energy is located in the minimum of the density of the states. Fig. 6b shows spin-polarized LDOS calculated for the magnetic SIA <110> configuration in bcc-Fe for one of two equivalent atoms in the dumbbell (denoted as 1: blue atom in Fig. 5b) and its nearest-neighbour atom (denoted as 2: light-red atom in Fig. 5b). VASP calculations show that atom 1 has a negative magnetic moment of $-0.25\ \mu_B$ in comparison with the positive value of $1.69\ \mu_B$ for the atom 2. Thus, the stability of the <110> dumbbell is strongly correlated with the anti-ferromagnetic ordering of magnetic moments in the core of the defect, which is therefore also responsible for the fact that the structure of radiation defects in iron and steels is different from the structure of defects formed under irradiation in the non-magnetic

body-centered cubic metals, for example vanadium or tungsten. This striking feature explaining the specificity of Fe, has been recently also found from DFT calculations in the SIA clusters with C15 Laves phase structures where the local magnetic moments in these clusters are fully anti-ferromagnetic with respect to the bulk bcc super-cell [48].

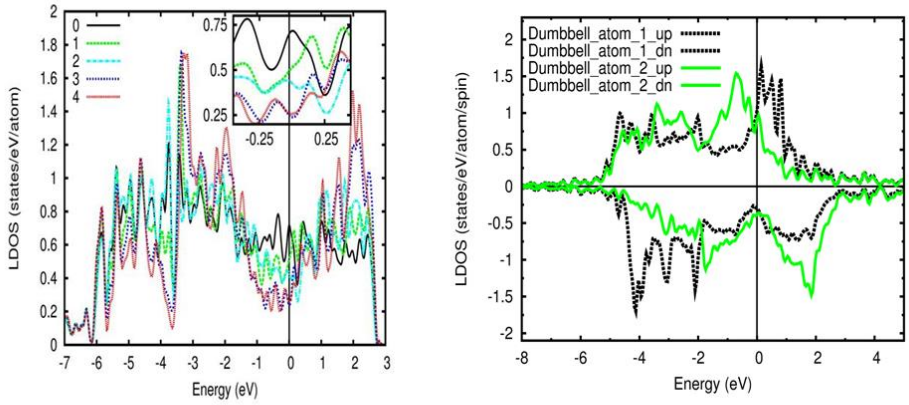

a) b)

Fig.6. Local electronic density of states for a) a <111> crowdion in bcc-W and b) a <110> dumbbell in bcc-Fe.

We should add here that our DFT predictions for the mono-vacancy formation and migration energies in all the bcc metals are also in a very good agreement with the available experimental data. For instance, the predicted high vacancy formation (3.5 eV) and vacancy migration (1.8 eV) energies result in high activation energy for self-diffusion in W alloys, which is in turn fundamentally responsible for the exceedingly long timescales characterizing kinetic phase transformation processes involving microstructural evolution of W-based alloys under irradiation.

Structural phase stability of iron and tungsten alloys derived from first-principles calculations

MCE modelling of Fe-Cr alloys

Fe–Cr alloys form the basis of many industrial steels. Ferritic/martensitic steels with 7–12 wt% Cr are candidate materials for the internal structures of future fusion power plants because of their remarkable resistance to swelling, and their adequate mechanical properties (tensile, impact and creep resistance up to 550^0 C) [49-50]. At the same time these steels suffer from radiation hardening and embrittlement below 400◦C even at moderate irradiation doses. In order to facilitate the use of these steels, it is necessary to understand the factors driving the evolution of microstructure, which is linked to the degradation of mechanical properties, and to access their structural stability during neutron irradiation or long thermal aging. It is in the context of this research programme that binary Fe–Cr alloys are studied as a model system, from which the fundamental mechanisms of radiation damage can be investigated and quantified. For applications it is important to understand the difference between magnetic and thermodynamic properties of Fe-Cr systems and precipitations of those containing more than 10%Cr. Our first-principles spin-polarized calculations of Fe-Cr alloys with various Cr content performed using 4x4x4 bcc-supercells show that clustering of Cr atoms occurring in alloys containing more than 12.5%

chromium is associated with the formation of anti-ferromagnetic phase of bcc-Cr [30]. Here, we investigate, using large-scale Monte-Carlo simulations, the effects of magnetic ordering of Fe-Cr alloys with large Cr content, especially systems with Cr precipitates and those containing atomically sharp Fe-Cr interfaces. For modeling the alloys, we use the recently developed *ab initio* based Magnetic Cluster Expansion (MCE) approach to modeling pure Fe and Fe-Cr alloys, which has recently been applied to modeling microstructure of the alloys in a broad range of Cr concentrations *and* temperatures [34-35, 51]. In particular, Monte Carlo simulations based on the MCE Hamiltonian parameterized in [34-35] make it possible to investigate finite temperature magnetic order and thermodynamic properties of alloys in a broad range of alloy compositions.

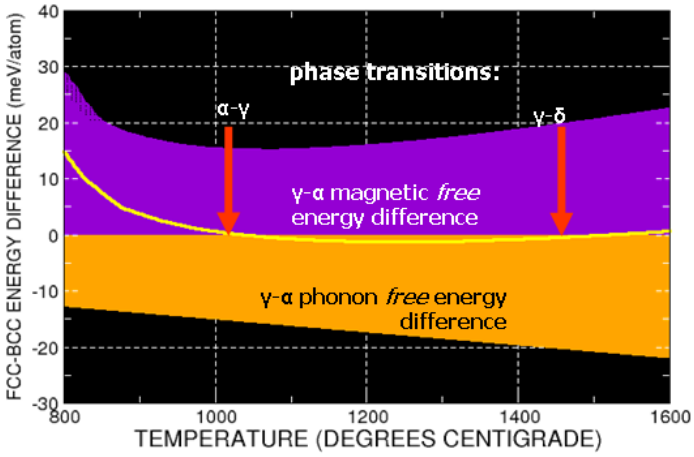

Fig.7. Diagram illustrating an MCE model prediction of bcc-fcc instability of iron at elevated temperatures.

Our *ab initio*-based MCE treatment developed for body- and face-centred cubic phases of iron and iron-chromium alloys is applied to modelling the α-γ and γ-δ phase transitions in these materials. The Curie, Néel, and the structural phase-transition temperatures predicted by the model are in good agreement with experimental observations, indicating that it is the thermal excitation of *both* magnetic *and* phonon degrees of freedom that stabilizes the fcc γ-phase. The model also describes the occurrence of the γ- loop in the phase diagram of Fe-Cr alloys for a realistic interval of temperatures and Cr concentrations. Fig. 7 illustrates the free energy differences between bcc and fcc phases as a function of temperature in pure iron, taking into account the two main contributions to the free energy, coming from magnetic and vibrational (phonon) excitations. The structural phase transition temperatures predicted by the MCE model are within 10% of the experimentally observed values. For example, we find that $T_{\alpha\gamma}^{MCE} = 1315\,K$ and $T_{\lambda\delta}^{MCE} = 1795\,K$ compared to $T_{\alpha\gamma}^{\exp} = 1185\,K$ and $T_{\lambda\delta}^{\exp} = 1667\,K$, respectively. The minimum value for the fcc-bcc free-energy difference predicted by the MCE model is very small and close to −2 meV/atom, in agreement with thermodynamic analysis [52-53] based on experimental information.

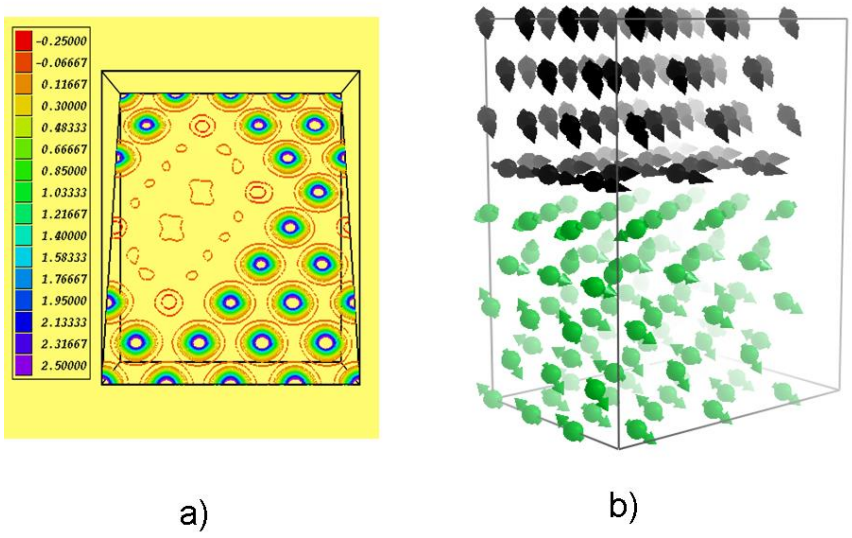

Fig.8. Magnetic properties of Cr clustering configuration at the (110) interface predicted by spin-polarized density from DFT calculations (a) and by non-collinear MCE simulations.

The clustering of bcc-Cr (α' phase) driven by magnetism in Fe-Cr alloys is shown in Fig. 8a using DFT spin-polarized magnetic map calculated for the 37.5%Cr configuration, which is found by combining Monte-Carlo simulation with cluster expansion Hamiltonian (1). The formation of a Cr cluster bounded by the (110) planes is consistent with large-scale Monte Carlo simulations showing large Cr clusters separated from the surrounding Fe matrix by interfaces parallel to the (110) crystallographic planes [18]. Fig. 8b shows the non-collinear magnetic structure across the Fe/Cr (110) interface predicted by the MCE simulations [37]. Comparison with DFT non-collinear magnetic calculations shows that there is no fundamental disagreement between the two approaches.

First-principles modelling of W-Ta and W-V alloys

Using *ab initio* methods, we have carried out a comprehensive DFT and CE investigation of phase stability and mechanical properties of W-Ta and W-V alloys, which are candidate materials for fusion power plant applications [19-20]. The experimental phase diagrams of W-Ta and W-V alloys show that these binaries exhibit full solubility in bcc α phase up to the solidus line, showing no occurrence of intermetallic phases [54-56]. Still, experimental results indicate that solid W-Ta alloys exhibit deviations from the ideal solid solution behaviour in the temperature range between 1050 and 1200 K [57]. The first-principles calculations have confirmed that these alloys are characterized by the negative enthalpy of mixing across the entire composition range. Importantly, complex intermetallic compounds are predicted as the ground-state structures for both alloys with W_5Ta_3 having the lowest enthalpy of mixing of −117.1meV/atom and the $C11_b$ (W_2V) of −92.9 meV/atom for W-Ta and W-V, respectively. The corresponding maximum order-disorder temperature derived from Monte Carlo simulations is close to 600 K for W-Ta alloys and to 250 K for W-V alloys.

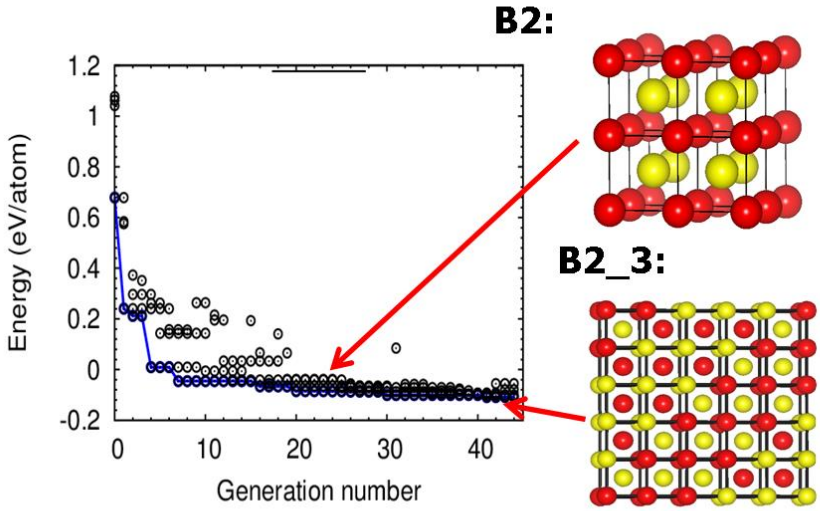

Fig 8. Ground-state prediction of inter-metallic phase in WTa alloy using an evolution algorithm.

From first-principles evaluation of effective CE interactions [19], we find that the first nearest-neighbour (1NN) pair interactions are positive and dominant in both cases, implying that the 1NN effective cluster interaction strongly favour *A*-*B* chemical mixing. The sign of the second-nearest-neighbour (2NN) pair interaction varies; it is negative (−10.704 meV) for W-Ta and positive (+34.992 meV) for W-V. This means that the 2NN atomic environments in W-Ta and W-V alloys are dissimilar and this difference is particularly pronounced for 50% tungsten alloys. For example, the $B2_3$ structure (see Fig. 8), where the 2NN atoms form pairs of *A*-*A* or *B*-*B* type, is predicted as intermetallic compound for the WTa binary, whereas the *B*32 structure, where the 2NN atom pairs are of *A*-*B* type, is found for the W-V alloy. The prediction of $B2_3$ inter-metallic phase in the W-Ta alloys agrees with other CE calculations [58]. $B2_3$ is a close relative of the *B*2 structure (see Fig. 8), but with an ordered array of antiphase boundaries in every third 110 plane. Very recently, we used unconstrained structural optimization combined with *ab initio* evolutionary algorithms (EA) to accelerate the search for complex inter-metallic phases at a given composition [59-60]. Fig. 8 shows enthalpy distributions for competing structures during an EA-driven ground state search for 1:1 W-Ta composition. After only 44 generations, the evolution search finds the ground-state structure $B2_3$ which has a lower enthalpy of mixing than the *B2* structure, in full agreement with our earlier predictions derived from CE and Monte-Carlo simulations.

DFT prediction of anisotropic elasticity of alloys

Understanding mechanical properties of irradiated iron and iron-based alloys, in particular, the relative stability of the a[100] and (a/2)[111] prismatic edge dislocation loops formed during irradiation [61] has been recently advanced by full anisotropic elasticity treatment [62]. The orientation dependence of Young modulus in Fe-Cr and W alloys [19-20] were investigated from fully relaxed and optimized structures obtained from DFT total energy calculations of elastic constants. For a single crystal, Young's modulus in a particular crystallographic direction is defined as follows. When a tensile stress is applied in that direction, the ratio of the stress to the tensile strain in that direction gives the Young modulus. Fig. 9 shows the predicted behaviour of relative anisotropic Young modulus for Fe-25%Cr alloy with respect to its value in the [100] direction found from our DFT calculations of elastic constants. The calculated values are compared with those obtained from experimental data of elastic constants for Fe-20%Cr alloys [63]. There is an excellent agreement between DFT and experimental behaviour showing that the Young modulus has a strong maximum in the [111] crystallographic direction. Fig. 9 also shows the variation of anisotropic Young modulus surfaces for corresponding Fe-Cr alloys visualized by colour code [64]. Each point on the given surface represents the magnitude of Young modulus in

the direction of a vector from the origin to the given point on the surface. Again there is a very good agreement of the absolute Young modulus data between first-principles calculations and experimental values. For W-Ta and W-V alloys, the values of the Young modulus and the Poisson ratio, as well as the empirical Rice-Thompson criterion for the ground-state structures and several metastable cubic alloy structures were used for assessing the effect of alloying on mechanical properties and the effect of chemical composition on ductility.

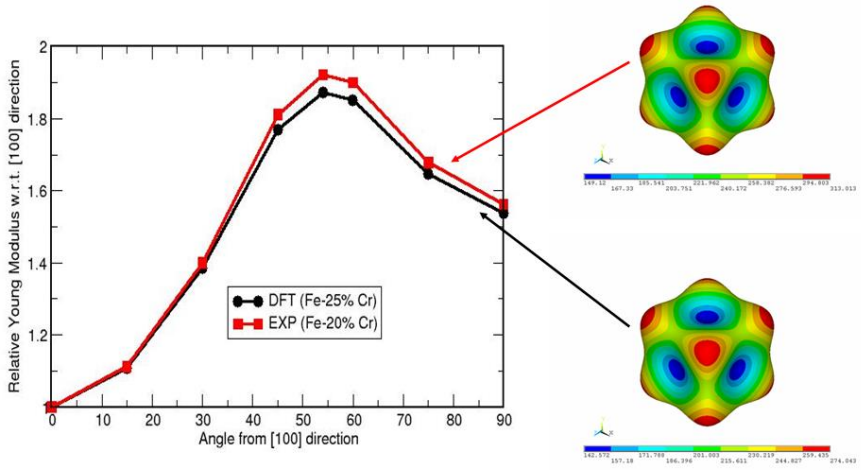

Fig.9. Results of first-principles calculations compared with experimental data on anisotropic elastic properties of Fe-Cr alloys.

Theoretical investigation of Debye temperature in Fe-Cr alloys was stimulated by the recent experimental works using Mossbauer spectroscopy, carried out on the Fe sub-lattice matrices in both bcc and sigma phases [65-66]. We have carried out systematic calculations of elastic constants from where the Debye temperature was derived using the calculated values of sound velocities for the both phases in Fe-Cr alloys. The Debye temperature (Θ_D) of 466K was predicted for ferromagnetic bcc-Fe as compared with the experimental value of 470K, whereas in bcc-Cr anti-ferromagnetic phase it was found that Θ_D=615K compared with the experimental value of 630K [67]. Fig. 10 shows the calculated Θ_D at 40, 53.3 and 66.7 %Cr in Fe-Cr σ-phase. We found the increase of the Debye temperature as a function of Cr concentration in very good agreement with the experimental trend found from the Mossbauer spectra measurements [65]. We note that in Mossbauer experiments, the hyperfine spectra measurements in Fe-Cr alloys are related to the change Fe sub-lattice magnetic properties and therefore the measured values of the Debye temperature are lower than those predicted and shown in Fig. 10, because of the missing contribution to the Debye temperature from the Cr sub-lattice.

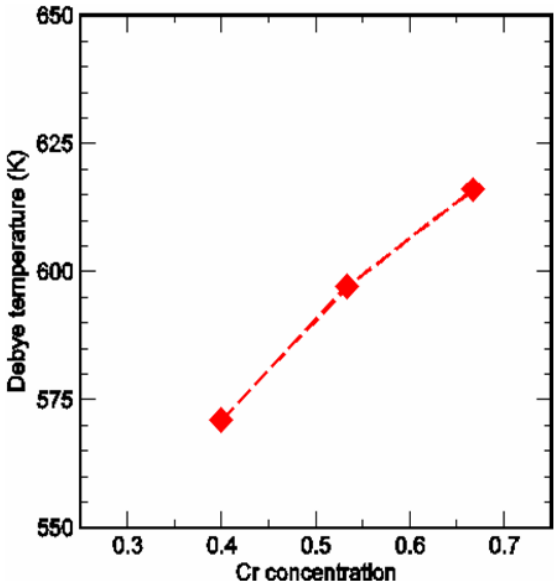

Fig.10. DFT prediction of the Debye temperature in Fe-Cr σ-phase

Point defect behaviour in iron and tungsten alloys

One of the most reliable methods for modeling alloy microstructure, phase decomposition and precipitate growth on a long time scales, such as the effect of α-α' phase separation in Fe–Cr alloys, is kinetic Monte Carlo (kMC) algorithm. A challenge associated with using this algorithm is related to the environmental dependence of the migration energy barriers for the atom-defect exchange [31,51]. Currently, there are several models for the environmental dependence of migration energy barriers, which are based either on the Kahn-Weinberg decomposition, the use of artificial neural networks, or the broken bond approximation [68]. All these models, whilst giving qualitatively similar results in agreement with experiment, have various drawbacks. The broken bond approximation, based on the CE model for Fe-Cr without defects [18], seems too crude for a quantitative description of a system with a vacancy. The Kahn-Weinberg decomposition and the artificial neural network (ANN) approaches, while giving better results, are based on vacancy migration energies calculated using empirical potentials and are less reliable than DFT. Fig. 11 shows cross-checking of configurations encountered during an atomistic kMC run employing ANN approach compared with those recalculated with the so-called two-band model (2BM) empirical potentials and our DFT using the Nudge Elastic Band (NEB) method. The comparison has been done for 10 different configurations with high and low mono-vacancy migration energy, $E_{m,}$ in Fe-Cr alloys containing 20%Cr where experimental information about nano-particle size and density distribution for the α' precipitation is available [69-70]. We see that it is quite difficult to reproduce the environmental dependence of migration energy barrier $E_{m,}$ predicted by first-principles calculations.

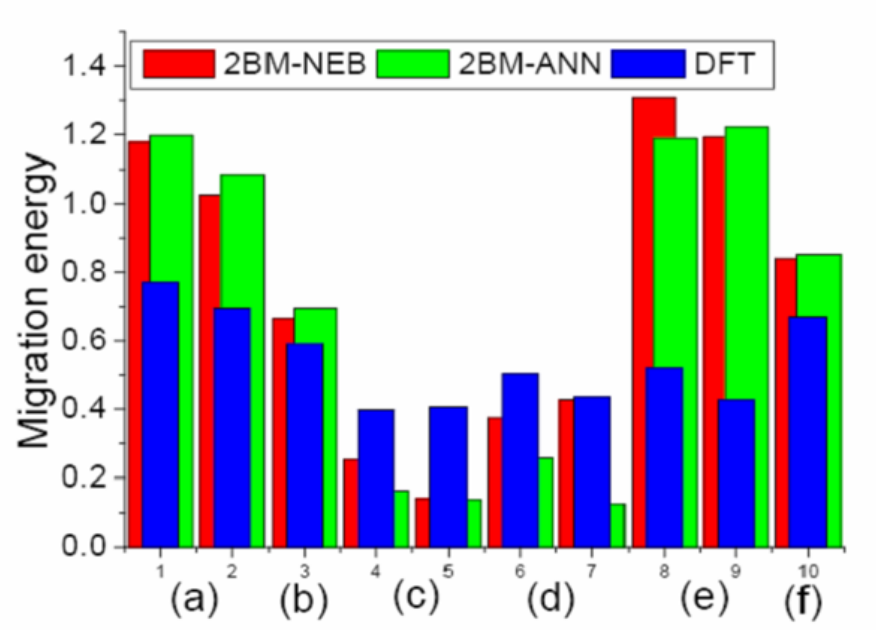

Fig.11. DFT predictions versus empirical potential models for vacancy migration energies in six different configurations in Fe-20%Cr alloys. The classification of these different configurations (a-f) is the same as in Fig. 1 of Ref. [68].

We showed that the CE method can be used to study the kinetics of the Fe–Cr system in atomistic kinetic Monte Carlo (AKMC). In bcc Fe-Cr system, the diffusion and precipitation processes are mostly vacancy-mediated. A schematic drawing illustrating atom-vacancy exchange is shown in Fig. 12. Energy profile for the migration pathway is also shown in Fig. 12, where the migration energy E_m is defined as the difference between the saddle point energy and the initial energy: $E_m = E_s - E_i$. CE for the migration energy is based on its decomposition into two components, as shown in Fig.12:

$$E_m = E_1 + E_2 = \left(E_s - \frac{E_i + E_f}{2} \right) + \left(\frac{E_f - E_i}{2} \right) \tag{5}$$

The first component here, namely the difference between the saddle point energy and the mean of the initial and final energies $E_1 = E_s - \left(E_i + E_f\right)/2$, coincides with the kinetically resolved activation barrier introduced in [71], and depends on the local atomic configuration around the migrating ion at the saddle point. This quantity can be described using a CE around the migrating atom in the saddle point. In bcc system the mid-point between the initial and final positions of the migration atom has 6 nearest neighbours, 6 second, and 8 third nearest neighbours [31]. The second component of the migration energy, the difference between the final and the initial energies $E_2 = \left(E_f - E_i\right)/2$, can be approximated using the CE similar to the one presented in [72]. In our case, we introduce vacancy formation energy as the difference between the energy of the crystal with a vacancy and the energy of the same crystal with the vacancy site occupied by *the same type of atom* as the one that is exchanged with the vacancy:

$$\Delta E_{i,f}(\sigma) = E_{i,f} - E(\sigma), \tag{6}$$

where $E(\sigma)$ refers to the initial or final configurations of the system but with a vacancy replaced by the atom of the same type σ as the atom that is being exchanged. This definition is particularly useful for the atom-vacancy exchange case, because in the expression for E_2 it involves only the vacancy formation energies for initial and final states, namely:

$$E_2 = \left(E_f - E_i\right)/2 = \left(\Delta E_f(\sigma) - \Delta E_i(\sigma)\right)/2 \tag{7}$$

The CE can now be constructed directly for the quantity E_2, so that one only needs to know the DFT values for the difference $E_f - E_i$. To find the value of E_1, atoms up to the fourth nearest neighbour of the vacancy were used in the CE [73].

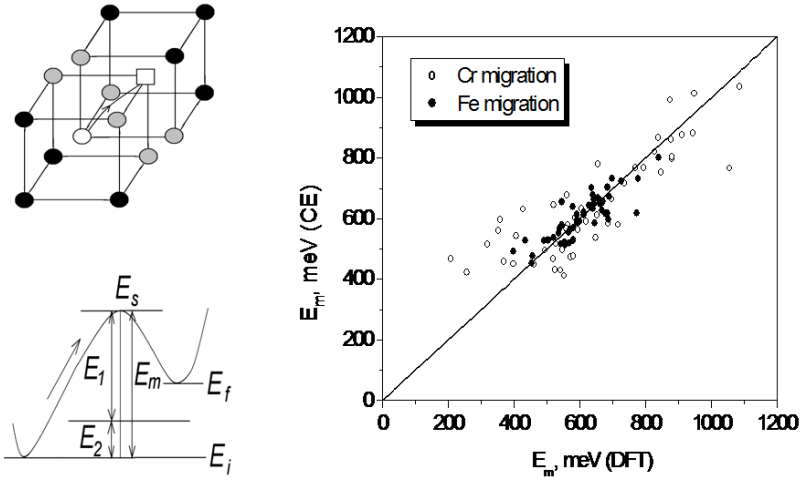

Fig.12. DFT validation of vacancy migration energy in Fe-Cr alloys using CE model.

A good overall agreement between DFT calculations and the CE model for almost all the concentrations, from pure Fe to pure Cr, and configurations studied with the mean error of not more than 0.1 eV [73] as shown in Fig. 12.

In order to clarify the origin of difference of migration energies predicted by DFT calculations with those obtained from empirical potentials (2BM), we have performed the analysis of spin-density maps for the saddle-point energy configurations. Fig. 13 shows the map for the case of migrating atom from the Fe atom site to the vacancy site. At the saddle-point position, the magnetic moment of Fe atom is -0.88 Bohr magnetons and it is aligned anti-ferromagnetically in comparison with Fe atoms in the matrix. This important feature obviously cannot be considered with the empirical potential treatment and again highlights the important role played by magnetism in point-defect diffusion in Fe-Cr alloys.

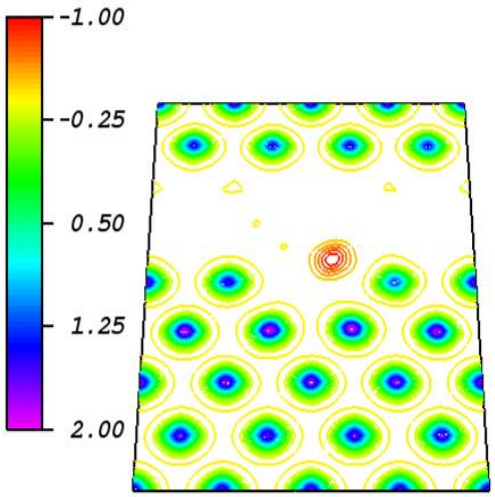

Fig.13. Spin density map for the saddle-point configuration showing negative magnetic moment of Fe migrating atom to a vacancy position in Fe-50%Cr alloys.

The time evolution can be followed as usual in kMC through the exchange frequency factor

$$\Gamma = \nu_0 \exp(-\frac{E_m}{k_B T}) \quad (8)$$

From DFT calculations for vacancy migration energies we found that E_m =0.64 eV for Fe-vacancy exchange and E_m =0.57 eV for Cr-vacancy exchange in bcc-Fe. We have now applied this CE method to the study of precipitate formation in an initially random Fe–20% Cr system, and found very good agreement with experiment and other methods [68]. The simulation box in that study consisted of 40x40x40 unit cells, or 128,000 lattice sites, and the evolution of the system was followed over a period of 0.782 s, which is equivalent to 4.4 x10^9 vacancy-atom exchanges at temperature T = 773 K. Fig. 14 shows a snapshot of the distribution of Cr atoms, taken after 0.569 s. A significant degree of precipitation from a random alloy is clearly visible, with number of clusters falling from seven at 0.284 s to four at 0.569s and two at 0.782 s [51]. Summarizing, the CE method allows both MC and kMC simulations, and can be used for studying both the equilibrium properties and the time evolution of the system.

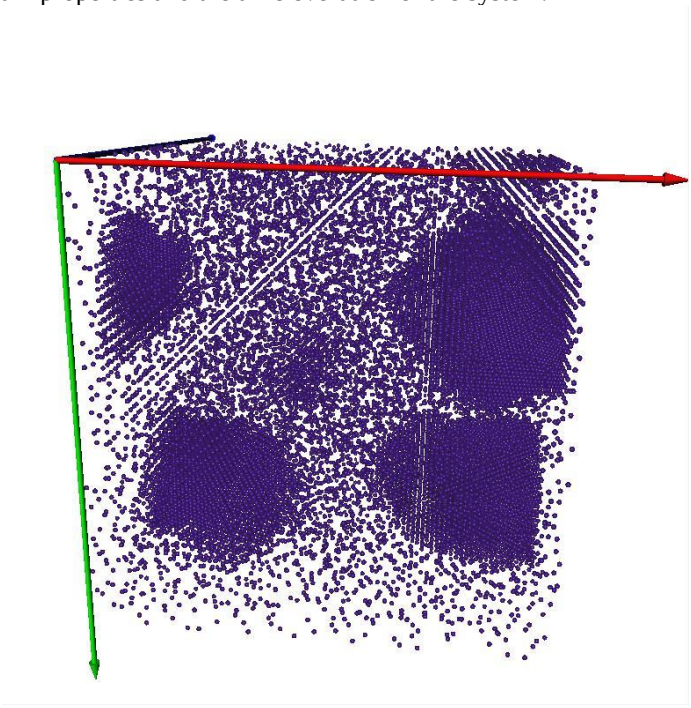

Fig.14. A snapshot of chromium clustering in Fe-20%Cr alloys obtained from kinetic Monte Carlo simulations using the CE model.

We have also computed mono-vacancy formation energies for a selected set of ground-state structures of W-Ta and W-V alloys as a function of tungsten concentration [19]. The vacancy formation energy for in W-Ta strongly depends on the environment of a vacancy site, varying by as much as 2 eV between Ta and W sites. The origin of the effect is likely associated with atomic volume mismatch between the tungsten and tantalum atoms. Our calculations are at variance with the results obtained recently for mono-vacancy formation energy in W-Ta using Virtual Crystal Approximation (VCA) where this environmental effect was ignored. By averaging over all configurations calculated from our DFT calculations at each composition, we found that the trend of VCA results corresponds to an approximation in which the hopping rate is evaluated using the average value of the mono-vacancy formation energy. The case of W-V alloys is very different in that we do not find any significant variation between the formation energies of vanadium or tungsten vacancies. Fig. 15 illustrates the strong environmental dependence of vacancy migration energy found for both W-Ta and W-V alloys.

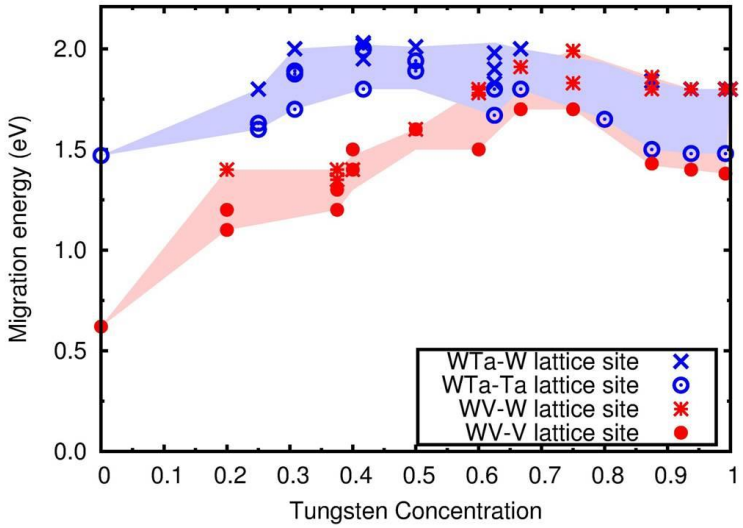

Fig. 15. Environmental dependence of migration energies for mono-vacancy in W-Ta and W-V alloys predicted using a combination of DFT calculations with CE model.

Finally, we have investigated the strength of interaction between a 〈111〉 SIA crowdion with Ta and V impurity atoms. We find that the binding energy is positive (attraction) for a defect in tungsten interacting with a vanadium atom, and that the binding energy is negative (repulsion) for a defect interacting with a tantalum atom [19]. In order to understand the origin of this difference, we analyse in Fig. 16 the LDOS calculated for the W atom located at the nearest neighbour to the central atom of crowdion. We found that the LDOS at the Fermi energy for the case of vanadium interacting with the SIA <111> string of crowdion is lower than those found for the intrinsic defect in pure W as well as in the case of Ta interaction. A <111> self-interstitial atom crowdion defect therefore binds to a vanadium solute atom essentially due to electronic structure effects [29]. At the same time, we note that there is an even simpler qualitative explanation that accounts for the observed trend in the interaction between a defect and an impurity atom in a dilute alloy. The effective volume of a vanadium atom is 13.8 A^3, which is smaller than the volume of a tungsten atom, which is 15.8 A^3. The latter is smaller than the effective volume of a tantalum atom, which is 18.1 A^3. Given that a self-interestitial defect is associated with a localized region of compression in the lattice, it is not unnatural that it is attracted to a smaller-size impurity atoms, and is repelled

by a large-size impurity atom.

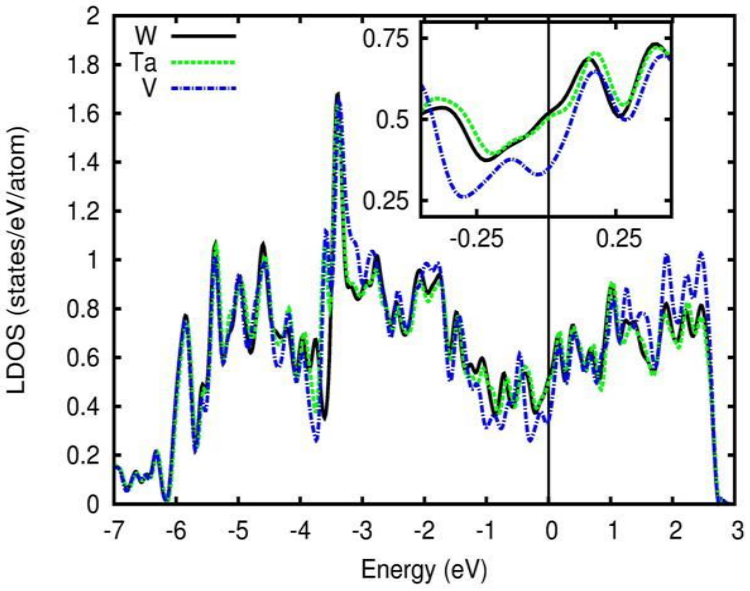

Fig. 16. Comparison between the local electronic DOS for an atom adjacent to the centre of the <111> crowdion configuration in pure tungsten with those calculated in the presence of Ta or V atom.

Conclusions

The development of new materials for plasma facing components, first wall and blanket systems of a future tokamak-based magnetically confined fusion power plant represents a formidable challenge for materials science and engineering. Micro-structural evolution of materials under irradiation is driven by the accumulation, migration and agglomeration of radiation-induced defects, as well as by their interaction with solute and impurity atoms. We have showed in this review that recent density functional theory (DFT) calculations can dramatically improve our understanding of the structure of defects formed in bcc transition metals and alloys under irradiation. We find that in ferromagnetic bcc iron a self-interstitial atom (SIA) defect adopts the <110>-type configuration, while in all the non-magnetic bcc transition metals, including vanadium and tungsten, an interstitial defect has a linear one-dimensional <111> structure. These two types of SIA defects are characterized by very different thermally activated mobilities. First-principles computations also play a crucial role in developing new algorithms associated with quantum mechanical calculations, such as many-body tight-binding Stoner model and Magnetic Cluster Expansion method which are capable of predicting the magnetic behaviour of materials under conditions not yet accessible to experimental tests in the fusion-relevant conditions. *Ab initio* prediction of phase stability, chemical bonding and environmental dependence of point defect configurations are also shown to be essential for understanding microstructural evolution of ferritic steels and tungsten alloys. Although first-principles approaches are currently only possible for systems involving a small numbers of atoms, the recent innovative developments in modelling techniques and improved high-performance and massive parallel computing platforms, as well as improved experimental characterization tools, will certainly help in providing means for developing self-consistent, experimentally validated models for materials performance in a fusion power plant environment.

Acknowledgements

This work, part-funded by the European Communities under the contract of Association between EURATOM and CCFE, was carried out within the framework of the European Fusion

Development Agreement. The views and opinions expressed herein do not necessarily reflect those of the European Commission. This work was also part-funded by the RCUK Energy Programme under grant EP/I501045. DNM would like to thank Dr. P. Norajitra for the permission to use his DEMO design sketch in Fig. 1 from the FZKA [74].

Reference

[1] A. Möslang, Comptes Rendus Physique **9**, 457 (2008)
[2] S.L. Dudarev, J.-L. Boutard, R. Lässer, M.J. Caturla, P.M. Derlet, M. Fivel, C.-C. Fu, M.Y. Lavrentiev, L. Malerba, M. Mrovec, D. Nguyen-Manh, K. Nordlund, M. Perlado, R. Schäublin, H. Van Swygenhoven, D. Terentyev, J. Wallenius, D. Weygand, F. Willaime, J. Nucl. Mater., **386-388**, 1 (2009); J.-L. Boutard, S.L. Dudarev, M. Rieth, Journ. Nucl. Mater. **417**, 1042 (2011)
[3] M. Rieth J.L. Boutard, S.L. Dudarev, T. Ahlgren, S. Antusch, N. Baluc, M.-F. Barthe, C.S. Becquart,L. Ciupinski, J.B. Correia, C. Domain, J. Fikar, E. Fortuna, C.-C. Fu, E. Gaganidze, T.L. Galán, C. García-Rosales, B. Gludovatz, H. Greuner, K. Heinola, N. Holstein, N. Juslin, F. Koch, W. Krauss, K.J. Kurzydlowski, J. Linke, Ch. Linsmeier, N. Luzginova, H. Maier, M.S. Martínez, J.M. Missiaen, M. Muhammed, A. Muñoz, M. Muzyk, K. Nordlund, D. Nguyen-Manh, P. Norajitra, J. Opschoor, G. Pintsuk, R. Pippan, G. Ritz, L. Romaner, D. Rupp, R. Schäublin, J. Schlosser, I. Uytdenhouwen, J.G. van der Laan, L. Veleva, L. Ventelon, S. Wahlberg, F. Willaime, S. Wurster, M.A. Yar, J. Nucl. Mater., **417**, 463 (2011).
[4] D. Nguyen-Manh, A.P. Horsfield, S.L. Dudarev, Phys. Rev. B, **73**, 020101 (2006).
[5] S.D. Kenny, A.P. Horsfield, Comp. Phys. Comm., **180**, 2616 (2009).
[6] P. Soin, A.P. Horsfield, D. Nguyen-Manh, Comp. Phys. Comm., **182**, 1350 (2011).
[7] G. Kresse and J. Hafner, Phys. Rev. B **47**, 558 (1993).
[8] G. Kresse and J. Furthmuller, Phys. Rev. B **54**, 11169 (1996).
[9] G. Kresse and J. Hafner, Comput. Mater. Sci. **6**, 15 (1996).
[10] D. Nguyen-Manh, S.L. Dudarev, A.P. Horsfield, J. Nucl. Mater., **367**, 257 (2007)
[11] M. Muzyk, D. Nguyen-Manh. K.J. Kurzydlovski, N.L. Baluc, S.L. Dudarev, Phys. Rev. B, **84**, 104115 (2011).
[12] P. Perdew, K. Burke, and M. Ernzerhof, Phys. Rev. Lett. **77**, 3865 (1996).
[13] P.M. Derlet, D. Nguyen-Manh. S.L. Dudarev, Phys. Rev. B, **76** 054107 (2007).
[14] Hartwigsen, S. Goedecker, and J. Hutter, Phys. Rev. B **58**, 3641 (1998).
[15] S.P. Fitzgerald, D. Nguyen-Manh, Phys. Rev. Lett., 101, 115504 (2008).
[16] P. Ehrhart, P. Jung, H. Shultz, and H. Ullmaier, in *Atomic Defects in Metals*, edited by H. Ullmaier Landolt-Bornstein New Series, Group III, Vol. 25 (Springer-Verlag, Berlin, 1991).
[17] C. A. van de Walle, CALPHAD, **33**, 266, 2009.
[18] M. Yu. Lavrentiev, R. Drautz, D. Nguyen-Manh, T. P. C. Klaver, and S. L. Dudarev, Phys. Rev. B **75**, 014208 (2007).
[19] M. Muzyk, D. Nguyen-Manh, K. J. Kurzydłowski,N. L. Baluc, and S. L. Dudarev, Phys. Rev. B **84**, 104115 (2011).
[20] D. Nguyen-Manh, M. Muzyk, K. J. Kurzydłowski, N. L. Baluc, M. Reith, and S. L. Dudarev, Key Eng. Mater. **465**, 15 (2011).
[21] D. Nguyen-Manh, S.L. Dudarev, Phys. Rev. B, 80, 104440 (2009).
[[22] P. W. Anderson, in *Solid State Physics*, edited by F. Seitz and D. Turnbull _Academic, New York, **14**, 99 (1963).
[23] B. Caroli, C. Caroli, and D. R. Fredkin, Phys. Rev. **178**, 599 (1969).
[24] A. Kotani and T. Yamazaki, Prog. Theor. Phys. **108**, 117 _1992.
[25] S.L. Dudarev, D. Nguyen-Manh, A.P. Sutton, Phil. Mag. B, **75**, 613 (1997).
[26] S. L. Dudarev, G. A. Botton, S. Y. Savrasov, C. J. Humphreys, and A. P. Sutton, Phys. Rev. B **57**, 1505 (1998).
[27] H. Hasegawa, M. W. Finnis, and D. G. Pettifor, J. Phys. F: Met. Phys. **15**, 19 (1985).
[28] G. Liu, D. Nguyen-Manh, B.-G. Liu, and D. G. Pettifor, Phys. Rev. B **71**, 174115 (2005).
[29] D. Nguyen-Manh, V. Vitek, and A. P. Horsfield, Prog. Mater. Sci. **52**, 255 (2007).
[30] D. Nguyen-Manh, M. Y. Lavrentiev, and S. L. Dudarev, J. Comp. Aid. Mater. Des. **14**, 159 (2007).
[31] D. Nguyen-Manh, M. Yu. Lavrentiev, and S. L. Dudarev, C. R. Phys. **9**, 379 (2008).
[32] D. Nguyen-Manh, M. Yu. Lavrentiev, S.L. Dudarev, Comp. Mater. Sci., **44**, 1 (2008)
[33] M. Mrovec, D. Nguyen-Manh, C. Elsasser, P. Gumbsch, Phys. Rev. Lett., **106**, 246402 (2011).
[34] M.Yu. Lavrentiev, S.L. Dudarev, D. Nguyen-Manh, J. Nucl. Mater., 386-388, 22 (2009).
[35] M. Yu. Lavrentiev, D. Nguyen-Manh, S.L. Dudarev, Phys. Rev. B, 81, 184202 (2010).

[36] M. Yu. Lavrentiev, **,** K. Mergia, M. Gjoka, D. Nguyen-Manh, G. Apostolopoulos, S.L. Dudarev, J. Phys: Conden. Mat., (2012) submitted for publication.
[37] M. Yu. Lavrentiev, R. Soulairol, Chu-Chun Fu, D. Nguyen-Manh,S. L. Dudarev, Phys. Rev. B, 84, 144203 (2011).
[38] I. Cook, Nature Materials, **5**, 77 (2006).
[39] J.L. Boutard, A. Alamo, R. Lindaum M. Rieth, C.R. Phys., **9**, 287 (2008).
[40] C. Domain and C. S. Becquart, Phys. Rev. B **65**, 024103 (2001).
[41] C.-C. Fu, F. Willaime, and P. Ordejon, Phys. Rev. Lett. **92**, 175503 (2004).
[42] P. Ehrhart, K. H. Robrock, and H. R. Schober, in Physics of Radiation Effects in Crystals, edited by R. A. Johnson and A. N. Orlov (Elsevier, Amsterdam, 1986), p. 63.
[43] G. J. Ackland and R. Thetford, Philos. Mag. A **56**, 15 (1987).
[44] D. Nguyen-Manh, M. Mrovec, S. Fitzgerald, Mater. Trans, **49**, 2497 (2008).
[45] I. M. Neklyudov, E. V. Sadanov, G. D. Tolstolutskaja, V. A. Ksenofontov, T. I. Mazilova, and I. M. Mikhailovskij, Phys. Rev. B, **78**, 115418 (2008).
[46] K. Arakawa, K. Ono, M. Isshiki, K. Mimura, M. Uchikoshi, and H. Mori, Science, **318**, 956 (2007).
[47] T. Amiro, K. Arakawa, and H. Mori, Phil. Mag. Lett., **91**, 86 (2011).
[48] M.-C. Marinica, F. Willaime, and J.-P. Crocombette, Phys. Rev. Lett., **108**, 025501 (2012).
[49] A. Koyama, A. Hishinuma, D.S. Gelles, R.L. Klueh, W. Dietz, K. Ehrlich, J. Nucl. Mater. **233–237**, 138 (1996).
[50] E.A. Little, D.A. Stow, J. Nucl. Mater**. 87,** 25 (1979).
[51] M.Yu. Lavrentiev, D. Nguyen-Manh and S.L. Dudarev, Comp. Mat. Sci. **49**, S199 (2010).
[52] Q. Chen and B. Sundman, J. Phase Equilibria **22**, 631 (2001).
[53] R. J. Weiss and K. J. Tauer, Phys. Rev., 102, 1490 (1956).
[54] S. V. Nagender Naidu, A. M. Sriramamurthy, M. Vijyakumar, and P. Rama Rao, *"V-W (Vanadium-Tungsten)," Phase Diagrams of Binary Vanadium Alloys*, edited by J. E Smith (ASM International, Materials Park, OH, 1989), pp. 313–317.
[55] *Binary Alloy Phase Diagrams*, edited by T. B. Massalski (ASM International, Materials Park, OH, 1990).
[56] *Binary Systems from Mn-Mo to Y-Zr, Band 17, Teil 4, Landolt-Bornstein: Numerical Data and Functional Relationships in Science and Technology, New Series*, compiled by Scientific GroupThermodata Europe (SGTE), Springer Verlag (2006).
[57] S. C. Singhal and W. L. Worrell, Metall. Trans. **4**, 895 (1973).
[58] 24V. Blum and A. Zunger, Phys. Rev. B **72**, 020104 (2005).
[59] A.R. Oganov, J. Chen, C. Gatti, Y.Z. Ma,Y.M. Ma., C.W Glass., Z. Liu, T. Yu, O.O. Kurakevych, V.L. Solozhenko, Nature (London**) 457**, 863 (2009).
[60] A. N. Kolmogorov, S. Shah, E. R. Margine,1 A. F. Bialon, T. Hammerschmidt, and R. Drautz, Phys. Rev. Lett., **105**, 217003 (2010).
[61] B. C. Masters, Nature (London) **200**, 254 (1963); Philos. Mag. **11**, 881 (1965).
[62] S.L. Dudarev, R. Bullough, and P. M. Derlet, Phys. Rev. Lett. **100,** 135503 (2008)
[63] H. Massumoto and M. Kikuchi, Trans. JIM, **12**, 90 (1971).
[64] M. Muzyk, D. Nguyen-Manh, J. Wrobel, K.J. Kurzydlowski, N.L. Baluc, S.L. Dudarev, J. Nucl. Mater. (2012).
[65] B.F.O. Costa, J. Cieslak and S.M. Dubiel, J. Alloys and Compounds, **492**, L1, (2010)
[66] S. M. Dubiel, J. Cieslak, W. Sturhahn, M. Sternik, P., Piekarz, S. Stankov and K. Parlinski, Phys. Rev. Lett., **104**, 155503 (2010).
[67] C. Kittel, *Introduction to Solid State Physics*, 8th Edition, Berkeley, 2005.
[68] N. Castin, G. Bonny, D. Terentyev, M.Yu. Lavrentiev, D. Nguyen-Manh, J. Nucl. Mater., **417**, 1086 (2011).
[69] F. Bley, Acta Metall. Mater., **40** 1505 (1992) .
[70] S. Novy, P. Pareige, C. Pareige, J. Nucl. Mater., **384**, 96 (2009).
[71] A. Van der Ven et al., Phys. Rev. B **64**, 184307 (2001).
[72] A. Van der Ven and G. Ceder, Phys. Rev. B **71**, 054102 (2005).
[73] M.Yu. Lavrentiev, D. Nguyen-Manh and S.L. Dudarev, Proceedings of the Fifth International Conference "Multiscale Materials Modeling" (Freiburg, Germany, 2010), 703.
[74] P. Norajitra, L. Buhler, A. Buenaventura, E. Diegele, U. Fischer, S. Gordeev,, E. Hutter, R. Kruessmann, S. Malang, A. Orden, G. Reimann, J. Reimann, G. Vieider, D. Ward and F. Wasastjerna, *Conceptual design of the dual-coolant blanket within the framework of the EU power plant study* (TW2-TRP-PPCS12), Final report, FZKA 6780, May 2003.